Monthly Notices of the ROYAL ASTRONOMICAL SOCIETY

MNRAS **520,** 3974–3985 (2023) https://doi.org/10.1093/mnras/stad369
Advance Access publication 2023 February 2

A surprising abundance of massive quiescent galaxies at $3 < z < 5$ in the first data from *JWST* CEERS

A. C. Carnall [1]★ D. J. McLeod,[1] R. J. McLure,[1] J. S. Dunlop,[1] R. Begley [1] F. Cullen [1] C. T. Donnan [1] M. L. Hamadouche [1] S. M. Jewell,[1] E. W. Jones,[1] C. L. Pollock[1] and V. Wild [2]

[1]*SUPA, Institute for Astronomy, University of Edinburgh, Royal Observatory, Edinburgh EH9 3HJ, UK*
[2]*SUPA†, School of Physics and Astronomy, University of St Andrews, North Haugh, St Andrews KY16 9SS, UK*

Accepted 2023 January 31. Received 2023 January 1; in original form 2022 August 2

ABSTRACT

We report a robust sample of 10 massive quiescent galaxies at redshift, $z > 3$, selected using the first data from the *JWST* Cosmic Evolution Early Release Science programme. Three of these galaxies are at $4 < z < 5$, constituting the best evidence to date for quiescent galaxies significantly before $z = 4$. These extreme galaxies have stellar masses in the range $\log_{10}(M_*/\mathrm{M}_\odot) = 10.1$–$11.1$, and formed the bulk of their mass around $z \simeq 10$, with two objects having star formation histories that suggest they had already reached $\log_{10}(M_*/\mathrm{M}_\odot) > 10$ by $z \gtrsim 8$. We report number densities for our sample, demonstrating that, based on the small area of *JWST* imaging so far available, previous work appears to have underestimated the number of quiescent galaxies at $3 < z < 4$ by a factor of 3–5, due to a lack of ultra-deep imaging data at $\lambda > 2\,\mu$m. This result deepens the existing tension between observations and theoretical models, which already struggle to reproduce previous estimates of $z > 3$ quiescent galaxy number densities. Upcoming wider-area *JWST* imaging surveys will provide larger samples of such galaxies and more robust number densities, as well as providing opportunities to search for quiescent galaxies at $z > 5$. The galaxies we report are excellent potential targets for *JWST* NIRSpec spectroscopy, which will be required to understand in detail their physical properties, providing deeper insights into the processes responsible for forming massive galaxies and quenching star formation during the first billion years.

Key words: methods: statistical – galaxies: evolution – galaxies: star formation.

1 INTRODUCTION

Two of the most important outstanding questions in galaxy evolution are: when did the first galaxies begin to form stars, and when did the first galaxies quench their star formation activity? During the short time since the first data from *JWST* were released, remarkable progress has been made towards addressing the first of these questions. We now have good evidence that $\log_{10}(M_*/\mathrm{M}_\odot) \simeq 8$–$9$ galaxies were already in place by $z \simeq 17$, less than 250 Myr after the big bang, with preliminary evidence mounting that such objects are more numerous than expected (e.g. Castellano et al. 2022; Finkelstein et al. 2022; Naidu et al. 2022; Donnan et al. 2023). We have also uncovered the unexpectedly rapid growth of these early seeds into massive galaxies with $\log_{10}(M_*/\mathrm{M}_\odot) \simeq 10$–$11$ during the latter half of the first billion years, from $6 < z < 10$ (Labbe et al. 2022).

This extremely rapid assembly of the first massive galaxies is critically important for our understanding of quenching. If $\log_{10}(M_*/\mathrm{M}_\odot) \simeq 11$ galaxies already exist by $6 < z < 10$, these must equally rapidly quench, and remain quenched, to avoid becoming too massive to be accommodated by the lower-redshift galaxy stellar mass function (e.g. McLeod et al. 2021). This suggests massive quiescent galaxies at least as early as $z \simeq 6$.

Currently, the earliest spectroscopically confirmed massive quiescent galaxies are half a billion years later, when the Universe was $\simeq$1.5 Gyr old at $z \simeq 4$ (e.g. Glazebrook et al. 2017; Forrest et al. 2020; Valentino et al. 2020), and indeed it has proven extremely challenging to identify even robust photometric candidates at $z > 4$ (e.g. Merlin et al. 2018, 2019; Carnall et al. 2020; Esdaile et al. 2021; Santini et al. 2021; Stevans et al. 2021; Marsan et al. 2022). It is currently unclear whether this is due to an almost total lack of quiescent galaxies at earlier times, or due to a lack of ultra-deep, high-resolution imaging at $\lambda > 2\,\mu$m with which to constrain the Balmer break at these redshifts.

The number density and passive fraction of high-redshift massive galaxies are, however, key constraints on galaxy formation models, with current simulations unable to reproduce the observed number density of quiescent galaxies at $3 < z < 4$ (e.g. Schreiber et al. 2018; Cecchi et al. 2019; Girelli, Bolzonella & Cimatti 2019). This implies that key physics, capable of giving rise to extremely rapid quenching events, is still missing from these simulations. In this context, more robust constraints on the number density of massive quiescent galaxies at $3 < z < 4$, and confirmation of whether any such objects exist at $z > 4$, are key to our understanding of galaxy formation.

★ E-mail: adamc@roe.ac.uk
† Scottish Universities Physics Alliance.

By providing unprecedentedly deep infrared imaging at $\lambda > 2\,\mu$m, *JWST* opens up a unique opportunity to address this issue, promising the ability to robustly select representative samples of massive galaxies as far back as just a few hundred Myr after the big bang. In addition, its extremely high angular resolution (e.g. Suess et al. 2022) and wide-ranging spectroscopic capabilities (e.g. Carnall et al. 2023b) hold much promise for extending detailed studies of quiescent galaxy physical properties, such as star formation histories (SFHs), stellar metallicities and sizes, back to the first billion years. This endeavour has previously proven extremely challenging, even at cosmic noon (e.g. Wu et al. 2018; Belli, Newman & Ellis 2019; Carnall et al. 2019a, 2022; Beverage et al. 2021; Hamadouche et al. 2022).

In this paper, we use extremely deep $\lambda = 1$–$5\,\mu$m NIRCam imaging from the *JWST* Cosmic Evolution Early Release Science (CEERS[1]) programme (Finkelstein et al., in preparation) to search for massive galaxies at $z > 3$. In particular, we focus on constraining the number density of galaxies that have already quenched their star formation activity at this early time. We also make a first attempt at measuring the SFHs of these galaxies, despite the significant challenge of measuring these from photometric data alone, in order to link them with the extreme population of star-forming galaxies currently being uncovered during the first billion years. The spectroscopic capabilities of *JWST* mean that spectroscopic redshifts, SFR measurements, and even spectroscopic SFH and stellar metallicity determinations are a realistic prospect for these galaxies on a short time-scale (e.g. Carnall et al. 2023a).

The structure of this paper is as follows. In Section 2, we introduce the CEERS and ancillary data sets used in this work. In Section 3, we discuss our spectral energy distribution (SED) fitting methodology and sample selection. In Section 4, we present our results, including the discovery of three robustly identified massive quiescent galaxies at $4 < z < 5$. We discuss our results in Section 5 and present our conclusions in Section 6. All magnitudes are quoted in the AB system. For cosmological calculations, we adopt $\Omega_{\rm M} = 0.3$, $\Omega_\Lambda = 0.7$, and $H_0 = 70\,{\rm km\,s^{-1}\,Mpc^{-1}}$. We assume a Kroupa (2001) initial mass function, and assume the solar abundances of Asplund et al. (2009), such that $Z_\odot = 0.0142$.

2 DATA

The primary data set for this work is comprised of the first observations made as part of the CEERS survey (Finkelstein et al., in preparation) in the CANDELS Extended Groth Strip (EGS) field. We use data from the first four pointings observed in late June 2022. Imaging is available in seven NIRCam filters: *F*115*W*, *F*150*W*, *F*200*W*, *F*277*W*, *F*356*W*, *F*410*M*, and *F*444*W*, with integration times of 2635 s per filter, except *F*115*W* where the exposure time is doubled. The currently available CEERS data amount to a total effective area of $\simeq$30 arcmin^2 (e.g. Donnan et al. 2023).

In addition to the NIRCam imaging, we also make use of *Hubble Space Telescope* (*HST*) ACS data in the *F*435*W*, *F*606*W*, and *F*814*W* bands. We use the v1.9 EGS mosaics produced by the CEERS team (Koekemoer et al. 2011), which have a pixel scale of 0.03 arcsec.

We perform our own custom reduction of the NIRCam data, beginning with the Level 1 data products, using the PRIMER Enhanced NIRCam Image Processing Library (PENCIL), a custom version of the *JWST* pipeline (v1.6.2). We align and stack the individual reduced images using the SCAMP and SWARP codes (Bertin 2006, 2010). Our final mosaic images have a pixel scale of 0.03 arcsec in all bands. We PSF-homogenize all data to the *F*444*W* band using empirical PSFs derived from stacks of bright stars in our mosaic images. We make use of the CRDS_CTX = jwst_0942.pmap version of the *JWST* calibration files, released on 2022 July 28. We then apply the empirically derived, module-dependent calibration correction factors described in appendix C of Donnan et al. (2023). These calibrations are in good agreement with empirical calibrations derived by other teams.[2]

We employ the SExtractor code (Bertin & Arnouts 1996) to measure object photometry. We run SExtractor in dual image mode, with the *F*200*W* mosaic used as the detection image in all cases, as this is the wavelength range in which the SEDs of $z \simeq$ 3–5 quiescent galaxies peak. Fluxes are measured within 0.5 arcsec (16 pixel) diameter circular apertures. We then aperture-correct by scaling to measurements of FLUX_AUTO in the *F*200*W* band. This size of aperture is more than sufficient for our purposes, given that massive quiescent galaxies at high redshift are known to be both extremely compact and centrally concentrated (e.g. van der Wel et al. 2014).

We cut our catalogue at $F200W = 26.5$, at which magnitude objects have a typical *F*200*W* SNR $\simeq 20$. This is necessary to ensure objects are reliably detected with high SNR in the other relevant bands, in particular to obtain strong constraints on the Balmer break strength. This results in a parent sample of 10 542 objects.

We measure uncertainties for each object as the standard deviation of fluxes measured in the closest $\simeq$100 blank sky apertures (McLeod, McLure & Dunlop 2016), while masking out nearby objects, using the robust median absolute deviation estimator. We check the resulting photometry in the *F*606*W* and *F*814*W* bands by cross-matching with the CANDELS catalogue produced by Stefanon et al. (2017), finding good agreement (e.g. median offset of 0.07 mag in *F*814*W*, with a scatter of 0.14 mag).

3 METHOD

3.1 Spectral energy distribution fitting

The SED-fitting analysis in this work makes use of the BAGPIPES spectral fitting code (Carnall et al. 2018), and is based on the method used to search for $2 < z < 5$ massive quiescent galaxies in CANDELS UDS and GOODS South in Carnall et al. (2020).

The model we fit to our photometric data makes use of the Bruzual & Charlot (2003) stellar population models, in particular the 2016 updated version (Chevallard & Charlot 2016) using the MILES stellar spectral library (Sánchez-Blázquez et al. 2006; Falcón-Barroso et al. 2011) and the updated stellar evolutionary tracks of Bressan et al. (2012) and Marigo et al. (2013).

Nebular line and continuum emission are included in our model using an approach based on the CLOUDY photoionization code, outlined in section 3 of Carnall et al. (2018), following Byler et al. (2017). We assume an ionization parameter, $U = 10^{-3}$, and a lifetime for stellar birth clouds of 10 Myr.

Dust attenuation is included using the model of Salim, Boquien & Lee (2018), which has a variable slope, parametrized with a power-law deviation, δ, from the Calzetti et al. (2000) model. We allow the *V*-band attenuation, A_V, to vary from 0 to 8 mag. We further assume that light from stars still enclosed in stellar birth clouds and resulting nebular emission is attenuated by twice the A_V experienced by older

[1] https://ceers.github.io

[2] e.g. https://github.com/gbrammer/grizli/pull/107.

Table 1. The nine free parameters of the BAGPIPES model we fit to our photometric data (see Section 3), along with their associated prior distributions. The upper limit on τ, $t_{\rm obs}$, is the age of the Universe as a function of redshift. Logarithmic priors are all applied in base ten. For the Gaussian prior on δ, the mean is μ and the standard deviation is σ.

Component	Parameter	Symbol/unit	Range	Prior	Hyper-parameters
General	Redshift	z	(0, 20)	Uniform	
	Total stellar mass formed	$M_*/{\rm M}_\odot$	$(1, 10^{13})$	Logarithmic	
	Stellar and gas-phase metallicities	$Z/{\rm Z}_\odot$	(0.2, 2.5)	Logarithmic	
Star formation history	Double-power-law falling slope	α	(0.01, 1000)	Logarithmic	
	Double-power-law rising slope	β	(0.01, 1000)	Logarithmic	
	Double power-law turnover time	τ/Gyr	$(0.1, t_{\rm obs})$	Uniform	
Dust attenuation	V-band attenuation	A_V /mag	(0, 8)	Uniform	
	Deviation from Calzetti et al. (2000) slope	δ	$(-0.3, 0.3)$	Gaussian	$\mu = 0, \sigma = 0.1$
	Strength of 2175 Å bump	B	(0, 5)	Uniform	

stars within the wider interstellar medium (ISM) of the galaxy (e.g. Charlot & Fall 2000).

We assume a double-power-law SFH model, as introduced in Carnall et al. (2018, 2019b), which has been shown to reproduce well the SFHs of massive quiescent galaxies in the MUFASA simulation (Davé, Thompson & Hopkins 2016). The stellar and nebular metallicities of galaxies are assumed to be identical, and are varied with a uniform prior in logarithmic space from $-0.7 < \log_{10}(Z/{\rm Z}_\odot) < 0.4$. Intergalactic medium absorption is included using the model of Inoue et al. (2014). We vary redshift in our model with a uniform prior over the redshift range $z = 0$–20. A full list of the nine free parameters of our model and their associated prior distributions is given in Table 1. We fit our BAGPIPES model to the data using the MULTINEST nested sampling algorithm (Skilling 2006; Feroz et al. 2019), accessed via the PYMULTINEST interface (Buchner et al. 2014).

3.2 Selection of massive quiescent galaxies

We begin our selection process by requiring that objects have a posterior median redshift greater than $z = 3$. We also require that 97.5 per cent of the redshift posterior for each object lies above $z = 2.75$. This is in order to exclude objects with significant secondary low-redshift solutions, whilst retaining objects with narrow redshift posteriors that extend marginally below $z = 3$.

The sample is then cleaned by visual inspection of all 10 photometric bands, as well as the fitted BAGPIPES SEDs. We exclude objects that fall close to the edges of the NIRCam detector, objects for which coverage is only available in some bands, and various kinds of NIRCam detector artefacts (Rigby et al. 2022). We further exclude objects that are visible in short-wavelength imaging, below the position of the Lyman break at the BAGPIPES fitted redshift (which strongly implies the fitted redshift is incorrect). At the end of this process, we have a total of 421 galaxies at $z > 3$.

To separate star-forming and quiescent galaxies, we use a time-dependent cut in specific star formation rate (sSFR), as has been widely applied in the literature (e.g. Gallazzi et al. 2014; Pacifici et al. 2016). We define quiescent galaxies as those that have

$$\mathrm{sSFR} < \frac{0.2}{t_{\rm obs}}, \tag{1}$$

where $t_{\rm obs}$ is the age of the Universe at the redshift of the galaxy. This threshold is broadly equivalent to a selection in rest-frame UVJ colour space of $U - V > 0.88 \times (V - J) + 0.69$ (Carnall et al. 2018, 2019b) at all redshifts, which is the $z < 0.5$ quiescent galaxy selection criterion introduced by Williams et al. (2009).

Our full passive sample is defined as those for which the 50th percentile of the fitted BAGPIPES sSFR posterior distribution falls below this threshold. These objects are robustly placed at $z > 3$ by our fitting, and are more likely to be quiescent than star forming. However, we cannot confidently exclude star-forming solutions in all cases. Following Carnall et al. (2020), we then further define a 'robust' quiescent sub-sample, for which 97.5 per cent of the sSFR posterior is required to fall below the threshold in equation (1). For these robust objects, we exclude both low-redshift and star-forming solutions with high confidence.

By this process, we identify a total of 15 objects, 10 of which satisfy our robust selection criteria. We visually inspect the available *Spitzer*-MIPS 24 μm data (Dickinson & FIDEL Team 2007) for these objects to check for anomalously strong detections that would clearly indicate these are lower-redshift dusty star-forming galaxies; however, we do not find any obvious bright detections.

3.3 Comparison of our results with other codes

As an additional check on our results, we fit our photometry for these 15 objects with two additional SED fitting codes. We firstly run EAZY (Brammer, van Dokkum & Coppi 2008), using both the Pegase and principal component analysis template sets, and additionally run LEPHARE (Arnouts et al. 1999; Ilbert et al. 2006), using the Bruzual & Charlot (2003) models. The redshifts for these three spectral fitting runs, along with best-fitting masses and sSFRs from LEPHARE are provided in the online version of Table 2 as supplementary material.

For our robust sub-sample, all three additional sets of redshifts are in good agreement with our BAGPIPES results, with typical variations of $\mathrm{d}z \simeq 0.1$–0.2. The masses returned by LEPHARE are also very similar to our BAGPIPES posterior median values, with a mean offset of 0.07 dex. LEPHARE also returns sSFRs below the threshold defined in equation (1) for all 10 objects in our robust sub-sample.

For our five non-robust objects, the agreement is similar for four objects; however, for the remaining object (ID: 44362), LEPHARE finds a lower-mass star-forming solution, though all of the codes still find this object to be at $z \simeq 3$. This finding reflects the lower level of certainty we attach to objects that do not meet our robust selection criteria.

4 RESULTS

From our analysis, we identify a total of 15 quiescent galaxies at $z > 3$, of which 10 are members of our robust sub-sample. From these 15 objects, 4 are placed reliably at $z > 4$, and 3 of these are robustly identified as quiescent. This is the first clear identification

Table 2. Properties of the 15 massive quiescent galaxies at $z > 3$ we identify in this work. We define $t_{\rm form}$ as the age of the Universe corresponding to the mass-weighted age of each galaxy, and $z_{\rm form}$ as the corresponding redshift. For objects labelled as 'robust', we can confidently exclude star-forming solutions, whereas for non-robust objects the posterior median solution is quiescent, but we cannot confidently exclude star-forming solutions. Additional columns for this table, including spectral fitting results from EAZY and LEPHARE (see Section 3.3) are provided as supplementary online material.

ID	RA	Dec.	*F*150*W*	*F*200*W*	Redshift	$t_{\rm form}$ (Gyr)	$z_{\rm form}$	$\log_{10}(M_*/{\rm M}_\odot)$	$U-V$	$V-J$	Robust
17318	214.808153	52.832201	27.33	25.73	$4.50^{+0.13}_{-0.10}$	$0.5^{+0.3}_{-0.2}$	$9.5^{+6.2}_{-2.9}$	$10.13^{+0.04}_{-0.04}$	$1.22^{+0.13}_{-0.09}$	$0.26^{+0.14}_{-0.15}$	True
28316	214.871228	52.845073	23.44	22.22	$3.53^{+0.12}_{-0.12}$	$1.6^{+0.1}_{-0.1}$	$3.8^{+0.2}_{-0.1}$	$10.84^{+0.04}_{-0.04}$	$1.06^{+0.03}_{-0.04}$	$0.57^{+0.12}_{-0.12}$	False
29497	214.760622	52.845322	22.95	21.57	$3.25^{+0.08}_{-0.08}$	$1.2^{+0.2}_{-0.3}$	$4.9^{+1.4}_{-0.6}$	$11.34^{+0.06}_{-0.06}$	$1.44^{+0.10}_{-0.06}$	$0.53^{+0.10}_{-0.08}$	True
36262	214.895614	52.856497	22.77	21.68	$3.26^{+0.09}_{-0.10}$	$1.2^{+0.2}_{-0.3}$	$4.8^{+1.2}_{-0.5}$	$11.06^{+0.12}_{-0.07}$	$1.11^{+0.10}_{-0.04}$	$0.11^{+0.09}_{-0.08}$	True
40015	214.853899	52.861358	25.25	23.23	$3.68^{+0.16}_{-0.20}$	$1.1^{+0.2}_{-0.2}$	$5.2^{+1.1}_{-0.6}$	$11.53^{+0.10}_{-0.10}$	$2.04^{+0.08}_{-0.08}$	$1.44^{+0.16}_{-0.15}$	False
42128	214.850568	52.866030	25.35	23.81	$4.19^{+0.12}_{-0.12}$	$0.4^{+0.3}_{-0.2}$	$10.8^{+8.2}_{-3.4}$	$11.06^{+0.07}_{-0.05}$	$1.48^{+0.14}_{-0.07}$	$0.65^{+0.13}_{-0.12}$	True
44362	214.879163	52.869187	25.32	24.48	$3.39^{+0.29}_{-0.14}$	$1.7^{+0.1}_{-0.2}$	$3.7^{+0.3}_{-0.1}$	$9.63^{+0.04}_{-0.03}$	$0.78^{+0.03}_{-0.03}$	$0.07^{+0.09}_{-0.08}$	False
52124	214.866027	52.884091	24.7	23.23	$3.38^{+0.19}_{-0.09}$	$1.2^{+0.3}_{-0.3}$	$4.8^{+1.2}_{-0.8}$	$10.81^{+0.11}_{-0.05}$	$1.52^{+0.05}_{-0.09}$	$0.76^{+0.14}_{-0.17}$	False
52175	214.866039	52.884255	23.84	22.31	$3.44^{+0.14}_{-0.08}$	$1.2^{+0.1}_{-0.2}$	$4.8^{+0.7}_{-0.3}$	$10.87^{+0.05}_{-0.02}$	$1.32^{+0.04}_{-0.10}$	$0.33^{+0.05}_{-0.10}$	True
75768	214.904841	52.935352	24.51	23.25	$3.31^{+0.10}_{-0.07}$	$1.3^{+0.2}_{-0.3}$	$4.6^{+1.2}_{-0.4}$	$10.48^{+0.07}_{-0.04}$	$1.25^{+0.07}_{-0.06}$	$0.30^{+0.08}_{-0.09}$	True
80785	214.915559	52.949026	24.76	23.96	$4.86^{+0.15}_{-0.16}$	$0.5^{+0.2}_{-0.2}$	$9.2^{+3.6}_{-2.1}$	$10.90^{+0.08}_{-0.05}$	$1.04^{+0.09}_{-0.04}$	$0.08^{+0.18}_{-0.08}$	False
8888	214.767258	52.817698	25.19	23.73	$3.49^{+0.17}_{-0.12}$	$1.2^{+0.2}_{-0.3}$	$4.9^{+1.1}_{-0.6}$	$10.54^{+0.12}_{-0.08}$	$1.34^{+0.06}_{-0.06}$	$0.43^{+0.12}_{-0.10}$	True
92564	214.957874	52.980293	24.9	23.35	$3.47^{+0.11}_{-0.10}$	$1.2^{+0.1}_{-0.1}$	$4.9^{+0.5}_{-0.4}$	$10.49^{+0.08}_{-0.04}$	$1.29^{+0.07}_{-0.07}$	$0.30^{+0.09}_{-0.11}$	True
97581	214.981800	52.991238	24.14	22.64	$3.46^{+0.10}_{-0.09}$	$1.0^{+0.2}_{-0.2}$	$5.5^{+1.0}_{-0.8}$	$10.81^{+0.06}_{-0.03}$	$1.35^{+0.07}_{-0.10}$	$0.40^{+0.05}_{-0.11}$	True
101962	215.039054	53.002778	26.39	24.85	$4.39^{+0.11}_{-0.14}$	$0.4^{+0.3}_{-0.2}$	$12.1^{+6.3}_{-4.5}$	$10.63^{+0.06}_{-0.04}$	$1.36^{+0.11}_{-0.07}$	$0.46^{+0.16}_{-0.11}$	True

of massive quiescent galaxies significantly beyond $z = 4$. We provide coordinates, photometric redshifts, magnitudes, and physical properties for the 15 quiescent galaxies we identify in Table 2. We present SEDs for our 10 robust objects in Figs 1 and A1. Cutout images for these 10 robust galaxies are presented in Fig. A2.

4.1 Robust massive quiescent galaxies at z > 4

SEDs and colour images for the three $z > 4$ objects in our robust sub-sample are shown in Fig. 1. All three of these display a strong Balmer break between the *F*200*W* and *F*277*W* bands, which provides a very strong constraint on their redshifts. They also exhibit well-constrained red spectral slopes in the rest-frame near-UV, indicating a lack of ongoing star formation, and blue spectral slopes in the longer-wavelength NIRCam bands, strongly ruling our lower-redshift dusty solutions. In this section we briefly discuss the observed properties of each object, before moving on to discuss their SFHs in Section 5.

4.1.1 Galaxy 17318

The highest-redshift robust quiescent galaxy in our sample is object 17318, with $F200W = 25.7$ and a photometric redshift of $z \simeq 4.5$. This galaxy, as shown in the top panel of Fig. 1, exhibits the characteristic triangular SED shape of post-starburst (PSB) galaxies at lower redshift (e.g. Wild et al. 2014), implying a recent, rapid fall in SFR (e.g. Wild et al. 2020; D'Eugenio et al. 2021). This is perhaps unsurprising, considering this object is observed just $\simeq$1.4 billion years after the big bang. For this galaxy, we derive a stellar mass of $\log_{10}(M_*/{\rm M}_\odot) = 10.13 \pm 0.06$, and a 2σ upper limiting sSFR (97.5th percentile) of $\log_{10}({\rm sSFR/yr}^{-1}) = -10.6$.

Our sample is shown on the rest-frame UVJ colour diagram in Fig. 2. Galaxy 17318 is the bluest (closest to the bottom-left) robust object shown in the central panel, just below the horizontal edge of the solid UVJ selection box, again highly consistent with lower-redshift PSBs (e.g. Belli et al. 2019; Carnall et al. 2019a). The locations of $z > 3$ quiescent galaxies on various other rest-frame colour selection diagrams (e.g. NUVrJ; Ilbert et al. 2013) will be explored in upcoming work by Gould et al. (in preparation).

This object is at a similar redshift to GOODSS-9209, the highest-redshift candidate identified by Carnall et al. (2020), which is the target of NIRSpec Cycle 1 observations (Carnall et al. 2023a). This new galaxy however is $\simeq 0.6$ dex less massive, and approximately 2 mag fainter at $\lambda = 2$ μm (GOODSS-9209 has $K_s = 23.6$).

This object is not included in the CANDELS catalogue of Stefanon et al. (2017). We measure a *F*150*W* magnitude for this object of 27.4, which is fainter than the 50 per cent point-source completeness limit calculated by Stefanon et al. (2017) in their *F*160*W* selection band of 27.23. It is therefore not surprising that this object was not included.

4.1.2 Galaxy 101962

The second-highest-redshift robust candidate we identify is object 101692 at $z \simeq 4.4$, shown in the middle panel of Fig. 1. It is slightly redder than 17318, and is the middle robust quiescent object shown on the UVJ diagram in the central panel of Fig. 2. In most respects however, this object is quite similar to our other $z > 4$ robust candidates. For this galaxy, we derive a stellar mass of $\log_{10}(M_*/{\rm M}_\odot) = 10.63^{+0.06}_{-0.04}$ (approximately 0.5 dex more massive than 17318) and a 2σ upper limiting sSFR of $\log_{10}({\rm sSFR/yr}^{-1}) = -9.9$.

This is the only one of our three robust $z > 4$ candidates to appear in the CANDELS EGS catalogue of Stefanon et al. (2017), having a match within 0.1 arcsec (ID: 23297). We show the CANDELS photometry for this object in blue in Fig. 3. This galaxy was only previously detected with 3σ significance in the WFCAM K_s band, and no data were available at all between $\lambda = 2.3$–3.0 μm, meaning virtually no constraint could be placed on the Balmer break. The median photometric redshift reported by the CANDELS team (following the method of Dahlen et al. 2013) is $z = 3.5$. However, the individual estimates from their different codes display considerable variance, with a 1σ range from $z = 2.45$–4.70.

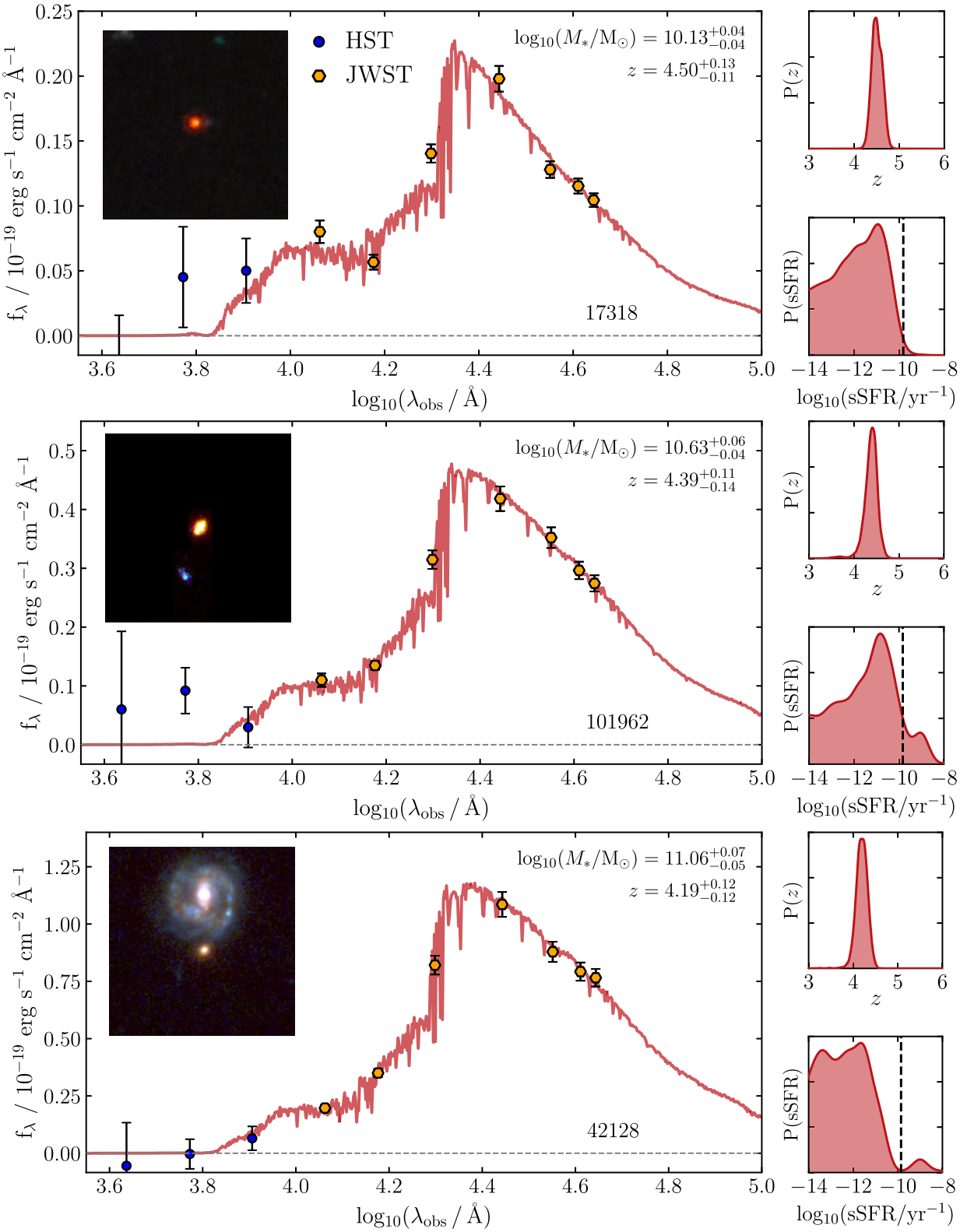

Figure 1. Spectral energy distributions and cutout images for our three robust $z > 4$ quiescent galaxies. Our 10-band photometric data from *HST* ACS and *JWST* NIRCam are shown in blue and gold, respectively. The posterior median BAGPIPES models are overlaid in red. Posterior distributions for the redshifts and sSFRs of these galaxies are shown to the right of the main panels. The dashed vertical lines in the sSFR panels show the sSFR threshold for inclusion in our quiescent sample at the redshift of each object (see Section 3.2). The inset RGB cutouts are composed of the *F*444*W*, *F*200*W*, and *F*150*W* images, respectively.

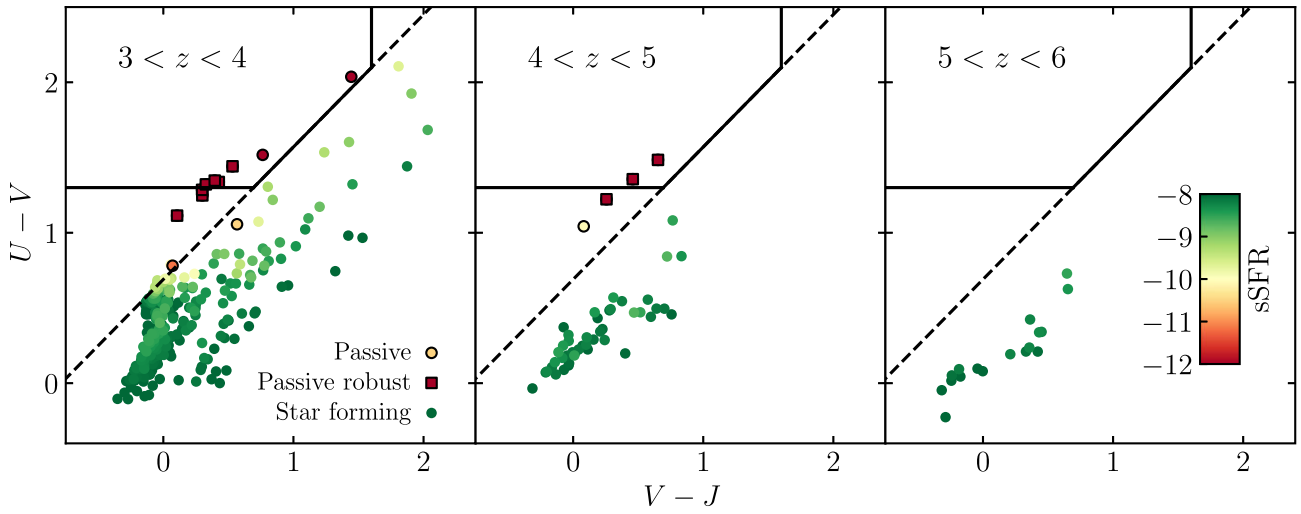

Figure 2. The rest-frame UVJ colour diagram, showing our magnitude-selected sample of massive galaxies ($F200W < 26.5$) in integer redshift bins spanning $3 < z < 6$. Points are coloured by sSFR, with star-forming galaxies denoted by circles without a border. Objects in our robust quiescent sub-sample are shown with black-bordered squares, whereas objects in our quiescent sample that do not meet our robust criteria (see Section 3.2) are shown as black-bordered circles. SEDs for the three robust quiescent galaxies we identify at $z > 4$ are shown in Fig. 1, whereas the seven robust quiescent galaxies at $3 < z < 4$ are shown in Fig. A1.

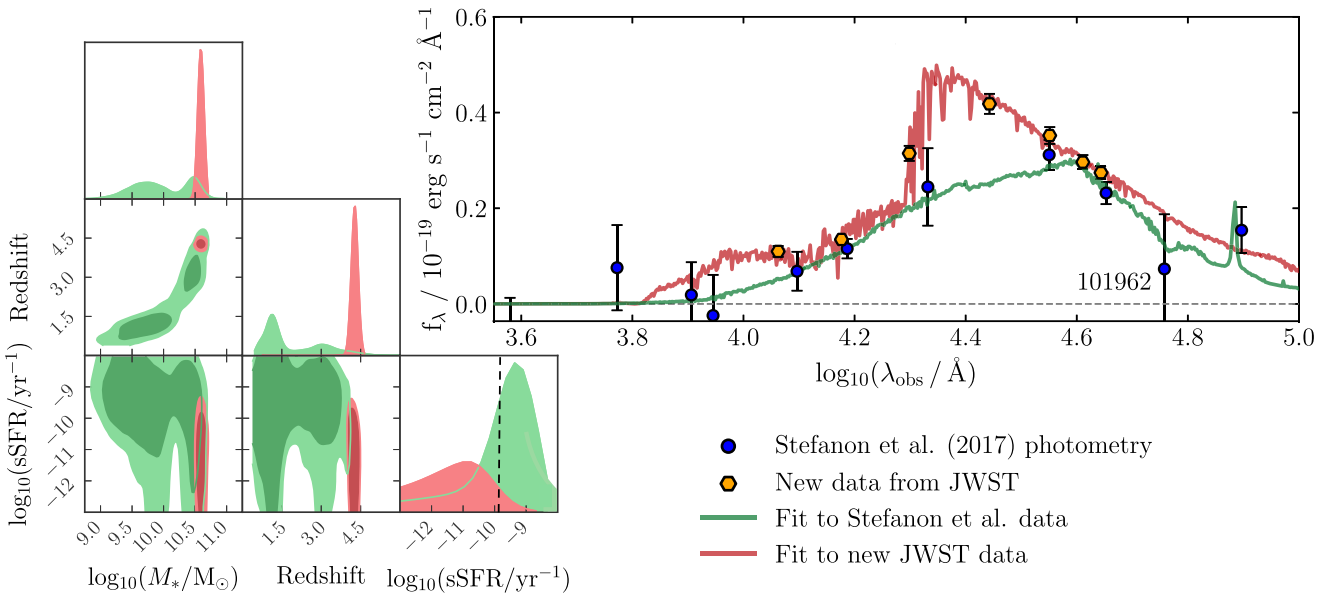

Figure 3. Comparison of pre-*JWST* and new *JWST* CEERS fit results for object 101962, the only robust $z > 4$ quiescent galaxy in our sample to be included in the CANDELS photometric catalogue of Stefanon et al. (2017). The best fit to the new *JWST* NIRCam data (gold) is shown in red, as in the middle panel of Fig. 1. The best fit to the CANDELS data (blue) is shown in green. The corner plot to the left shows constraints on the stellar mass, redshift, and sSFR of this galaxy from both data sets. It can be seen that previous data were unable to constrain these parameters, with an extremely large redshift uncertainty, $z = 1.34^{+1.94}_{-0.39}$. This is largely due to the low SNR of previous data, in particular around the Balmer break, and a lack of data at $\lambda \simeq 2.3$–3.0 μm between K_s and IRAC Channel 1.

As a demonstration, we fit the Stefanon et al. (2017) photometry shown in Fig. 3 with BAGPIPES, using the same model described in Section 3.1. Our best fit is shown in green in Fig. 3, along with the gold *JWST* data and red best fit from Fig. 1. From the Stefanon et al. (2017) data we recover an extremely broad photometric redshift posterior, $z = 1.34^{+1.94}_{-0.39}$. The 1D and 2D stellar mass, sSFR, and redshift posteriors for both fits are shown in the corner plot on the left side of Fig. 3. It can be seen that the lack of a well-constrained redshift results in a very broad stellar mass posterior, and virtually no constraint on the sSFR, with the sSFR posterior following the prior imposed by our SFH model (e.g. see fig. 1 of Carnall et al. 2019b).

4.1.3 Galaxy 42128

Galaxy 42128 has a slightly lower redshift, $z \simeq 4.2$, and is both brighter and more massive than the other two galaxies. It is also the reddest of our $z > 4$ candidates on the UVJ diagram. However, in most respects, this galaxy is very similar to 17318 and 101962, also

Table 3. Number densities derived for our quiescent galaxy sample in integer redshift bins spanning $3 < z < 5$. Uncertainties were calculated as the Poisson noise on the number of objects found (Gehrels 1986). The full quiescent sample includes quiescent galaxies for which we cannot rule out secondary star-forming solutions, whereas the robust sub-sample includes only those galaxies for which we can confidently exclude star-forming solutions.

Full quiescent sample			
Redshift range	$N_{\rm galaxies}$ $F200W < 26.5$	n (Mpc^{-3}) $F200W < 26.5$	n (Mpc^{-3}) $F200W < 24.5$
$3 < z < 4$	11	$11.6^{+4.7}_{-3.4} \times 10^{-5}$	$10.6^{+4.5}_{-3.3} \times 10^{-5}$
$4 < z < 5$	4	$4.7^{+3.7}_{-2.2} \times 10^{-5}$	$2.3^{+3.1}_{-1.5} \times 10^{-5}$
Robust sub-sample			
Redshift range	$N_{\rm galaxies}$ $F200W < 26.5$	n / Mpc^{-3} $F200W < 26.5$	n / Mpc^{-3} $F200W < 24.5$
$3 < z < 4$	7	$7.4^{+4.0}_{-2.7} \times 10^{-5}$	$6.3^{+3.8}_{-2.5} \times 10^{-5}$
$4 < z < 5$	3	$3.5^{+3.4}_{-1.9} \times 10^{-5}$	$1.2^{+2.7}_{-1.0} \times 10^{-5}$

exhibiting the characteristic triangular PSB spectral shape. For this galaxy, we derive a stellar mass of $\log_{10}(M_*/{\rm M}_\odot) = 11.06^{+0.07}_{-0.05}$, and a 2σ upper limiting sSFR of $\log_{10}({\rm sSFR/yr}^{-1}) = -11.2$.

In shorter-wavelength, lower spatial resolution imaging this object is not distinguishable from the extended structure of the nearby barred-spiral galaxy and therefore does not feature in the Stefanon et al. (2017) CANDELS EGS catalogue. However, the longer wavelength and higher spatial resolution imaging provided by JWST reveal this object as a brighter, redder, highly compact background source.

4.2 Comparison with previous work in the EGS field

A previous search for $z > 3$ massive quiescent galaxies in the EGS field was presented by Merlin et al. (2019), who analysed the CANDELS catalogue of Stefanon et al. (2017). In this section, we present a comparison with their results to demonstrate the power of the new *JWST* data. From our 15-object sample, 12 objects have matches in the Stefanon et al. (2017) catalogue, including object 101963 discussed in Section 4.1.2.

Merlin et al. (2019) identify 13 candidate $z > 3$ quiescent galaxies in the Stefanon et al. (2017) catalogue. From these, four objects fall within the area covered by our *JWST* CEERS catalogue (a further object falls within a gap between two NIRCam short-wavelength detectors). All four of these are also included in our sample (IDs: 28316, 36262, 52175, 75768). These are all at $z \lesssim 3.5$, and are the four brightest galaxies in our sample in the $F150W$ band. The other eight objects in our sample that also appear in the Stefanon et al. (2017) catalogue were not selected by Merlin et al. (2019), likely as a result of their relative faintness, which makes constraining redshifts, masses and sSFRs more challenging, as demonstrated in Fig. 3.

4.3 Quiescent galaxy number densities at $3 < z < 5$

In Table 3, we report our estimates of the number densities of quiescent galaxies over the redshift range $3 < z < 5$ that meet our $F200W < 26.5$ selection threshold. We report number densities based on both our full quiescent sample and our robust sub-sample. The numbers based on the robust sub-sample can be interpreted as conservative lower limits.

In Schreiber et al. (2018), the authors report a number density of $2.0 \pm 0.3 \times 10^{-5}$ Mpc^{-3} for a spectroscopic sample of quiescent galaxies at $3 < z < 4$ with $K_s < 24.5$. We compare our results with

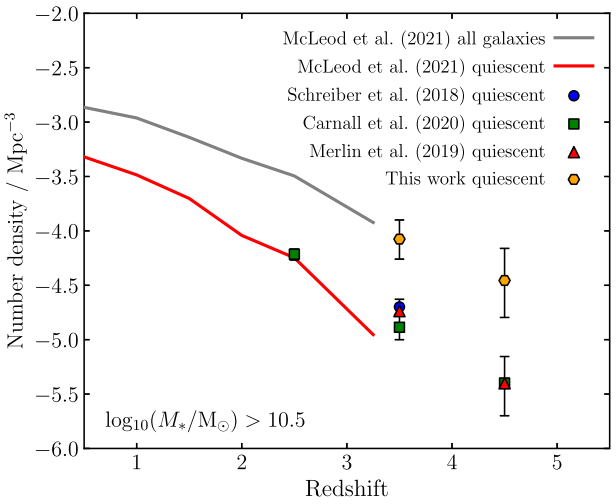

Figure 4. Number density estimates for high-redshift massive quiescent galaxies. Our estimate at $3 < z < 5$ derived from the *JWST* CEERS data are 3–5 times higher than pre-*JWST* estimates, and, at $z \simeq 3$, approach the result of McLeod et al. (2021) for the total galaxy population. Stellar masses derived by other authors have been converted to a Kroupa (2001) IMF where necessary.

Schreiber et al. (2018) by calculating the number of $F200W < 24.5$ quiescent galaxies in our sample at $3 < z < 4$, as this filter is closest in wavelength coverage to the K_s band. These numbers are reported in the right-hand column of Table 3.

The number density we find for our robust sub-sample at $F200W < 24.5$ is approximately a factor of 3 larger than the result of Schreiber et al. (2018), whereas the result from our full quiescent sample is approximately a factor of 5 larger. We attribute this significant increase in the number of $z > 3$ quiescent galaxies to the much deeper, redder imaging now available from *JWST*, which allows physical properties to be reliably inferred for faint, red galaxies such as these.

From our 11 quiescent galaxies at $3 < z < 4$, a total of 10 have matches within 0.25″ in the Stefanon et al. (2017) CANDELS EGS catalogue. From these 10, a total of 9 have CANDELS photometric redshifts in the range from $3 < z < 4$, and by fitting the Stefanon et al. (2017) photometry with BAGPIPES we recover similar results. However, just 3 of these objects would be included in our quiescent sample given the CANDELS photometry, as their sSFRs are far less well constrained by these data. Just 2 of these 3 would be identified as robust.

It is therefore likely that, had we designed a spectroscopic follow-up campaign similar to that of Schreiber et al. (2018) based on fitting only CANDELS EGS data, we would have arrived at a very similar number density for $3 < z < 4$ quiescent galaxies to the one they obtain. Indeed, our result based on fitting CANDELS UDS and GOODS South photometry in Carnall et al. (2020) arrived at a number density of $1.7 \pm 0.3 \times 10^{-5}$ Mpc^{-3} for $3 < z < 4$ quiescent galaxies with $K_s < 24.5$, fully consistent with Schreiber et al. (2018).

In Fig. 4, we show a comparison of $z > 3$ quiescent galaxy number density estimates from the literature, including our new results. We restrict this comparison to galaxies with $\log_{10}(M_*/{\rm M}_\odot) > 10.5$, where the CANDELS catalogues are mass complete at $z < 4$. At $z > 4$, the Balmer break moves to $\lambda > 2\,\mu$m, meaning selection at longer wavelengths is likely to be necessary to obtain mass-complete samples.

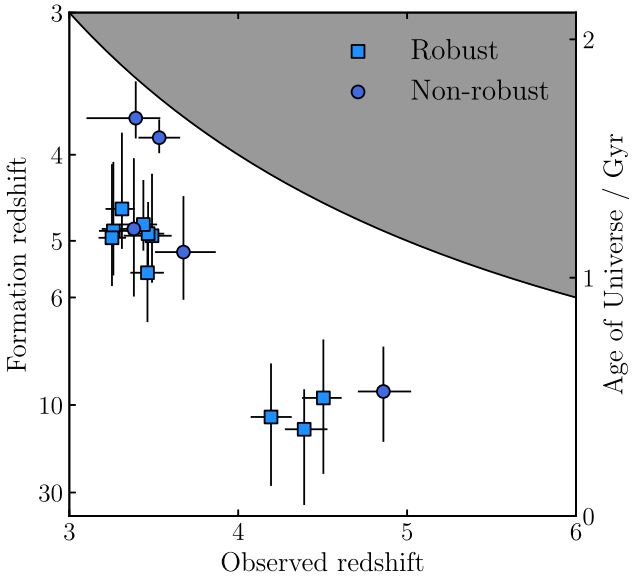

Figure 5. Formation redshifts for $z > 3$ massive quiescent galaxy sample, shown as a function of their observed redshifts. Our candidates at $z > 4$ have formation redshifts from $9 < z_{\rm form} < 12$, whereas our $3 < z < 4$ galaxies are all younger, having formed at $z_{\rm form} < 6$.

As above, it can be seen from Fig. 4 that our new result (for our full sample) is a factor of $\simeq$5 higher than previous estimates, which are all in close agreement. We also show results at $z < 3.75$ derived from the stellar mass functions of McLeod et al. (2021), both for quiescent galaxies and for the whole galaxy population. Our $3 < z < 4$ quiescent galaxy number density is close to the total number density found by McLeod et al. (2021). This suggests the small area studied in this work may be overdense at these redshifts.

Finally we note that, as shown in Carnall et al. (2019b), standard parametric SFH models impose strong priors on galaxy sSFRs, favouring sSFRs close to the star-forming main sequence. In the absence of strongly constraining data, this could plausibly result in quiescent galaxies being misidentified as star forming. This effect is demonstrated in Fig. 3, in which the sSFR posterior for galaxy 101962 using CANDELS data is strongly weighted towards star-forming solutions, even at the correct redshift of $z \simeq 4.4$. Clearly, follow-up studies using larger-area *JWST* imaging surveys are of critical importance to clarify this situation.

5 DISCUSSION

In this section, we discuss the star formation histories we infer for our sample. We calculate formation times, $t_{\rm form}$, for each object as the average time at which the stars in the galaxy formed. This is the age of the Universe at the time corresponding to the (mass-weighted) mean stellar age (see Carnall et al. 2018, equation 11). We also calculate formation redshifts, $z_{\rm form}$, which are the redshifts corresponding to $t_{\rm form}$. These values are reported in Table 2.

Formation redshifts for our sample are plotted against the observed redshift of each galaxy in Fig. 5. In addition, the full SFH posteriors for the 10 galaxies in our robust sub-sample are shown in Fig. 6. Their posterior median formation redshifts are shown with dashed grey vertical lines.

It can be seen that the three robust quiescent galaxies at $z > 4$ formed the bulk of their stellar populations during the first billion years at $z > 6$, with posterior median formation redshifts in the

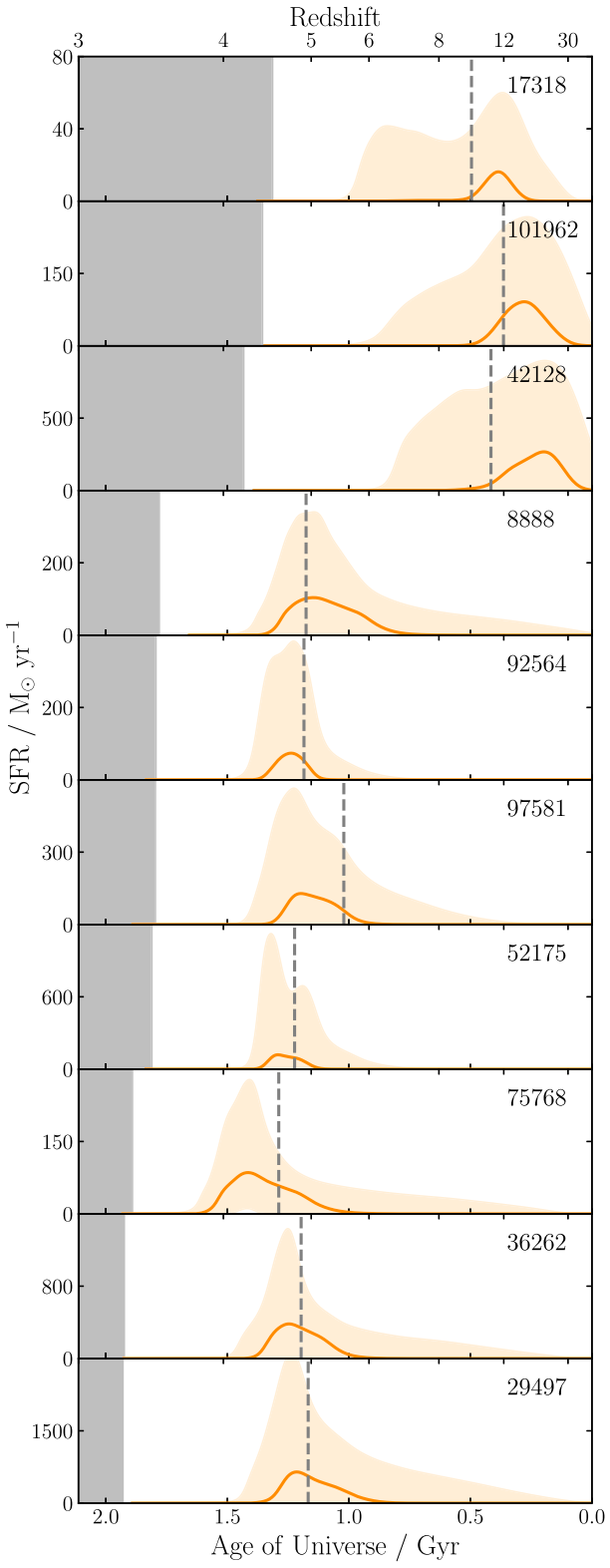

Figure 6. Star formation histories for our 10 robustly identified $z > 3$ quiescent galaxies. The solid orange lines show the 50th percentiles of the SFH posterior distributions in each case, whereas the orange shaded regions show the 1σ range. The dashed grey vertical lines show the posterior median redshift of formation for each object. SEDs are shown in Figs 1 and A1.

range $9 < z_{\rm form} < 12$. The second-highest-redshift object, 101962, is the earliest formed, with the bulk of its stars having formed at $z > 8$. These findings make our $z > 4$ objects highly plausible as descendants of the sample identified by Labbe et al. (2022). Indeed, objects 101962 and 42128 are both predicted to have had $\log_{10}(M_*/{\rm M}_\odot) > 10$ at their formation redshifts of $z_{\rm form} = 12.1^{+6.3}_{-4.5}$ and $z_{\rm form} = 10.8^{+8.2}_{-3.4}$, respectively. This is fully consistent with the finding of Labbe et al. (2022) that a considerable number of $\log_{10}(M_*/{\rm M}_\odot) > 10$ galaxies were already in place by $7 < z < 11$.

The seven robust quiescent galaxies at $3 < z < 4$ formed their stellar populations later in cosmic time, with $4 < z_{\rm form} < 6$. The fact that none of these galaxies is older suggests that the $z > 4$ quiescent galaxies in our sample have not yet reached the end-point of their evolution, and are likely to experience further star formation by $z \simeq 3$. However, larger-area *JWST* surveys and spectroscopic follow-up will certainly be required to rule out the possibility of $3 < z < 4$ quiescent galaxies with stellar populations dating back to $z > 6$.

It is interesting to reflect on the fact that we do not identify any quiescent galaxies at $z > 5$, despite the fact that our oldest object appears to have quenched by $z > 6$. Apart from the obvious limitations of the relatively small imaging area included in the initial CEERS release, it is currently unclear how the colours of newly quenched galaxies evolve in order to arrive in the UVJ-quiescent box, and how long this might take after star formation ceases (e.g. Belli et al. 2019; Carnall et al. 2019b; Akins et al. 2022).

Upcoming larger-area *JWST* imaging surveys, such as Public Release Imaging for Extragalactic Research (PRIMER[3]) are ideally suited to searching for evidence of quiescent galaxies at $z > 5$, as well as selecting larger samples of $3 < z < 5$ quiescent galaxies to produce more robust number densities. Such searches may benefit from the use of catalogues selected in longer-wavelength NIRCam bands, rather than the *F*200*W* selection employed in this work, as well as new, *JWST*-specific colour selection criteria (e.g. Leja, Tacchella & Conroy 2019; Antwi-Danso et al. 2022).

6 CONCLUSION

In this work, we present the results of a search for massive quiescent galaxies at redshifts $z > 3$, selected from the first NIRCam data taken by the *JWST* CEERS Early Release Science programme. We identify 15 galaxies in the redshift range $3 < z < 5$ with robust photometric redshifts and posterior median sSFRs that suggest they are quiescent. For 10 of these galaxies, we can confidently rule out star-forming solutions, and we refer to these galaxies as comprising our robust sub-sample.

Three of our robustly quiescent objects are at $z > 4$, and these constitute the best evidence to date for the existence of massive quiescent galaxies significantly above $z = 4$. These objects have stellar masses in the range $\log_{10}(M_*/{\rm M}_\odot) = 10.1$–$11.1$ and posterior median formation redshifts from $9 < z_{\rm form} < 12$. Two of these $z > 4$ galaxies would have had stellar masses in excess of $\log_{10}(M_*/{\rm M}_\odot) = 10$ by $z \gtrsim 8$, supporting the recent findings of Labbe et al. (2022).

Only one of these $z > 4$ objects has a match in the Stefanon et al. (2017) CANDELS EGS catalogue. The redshift of this object was not well constrained by previously available data, with both the CANDELS team and BAGPIPES returning extremely broad redshift posteriors, with best-fitting values at $z < 4$.

We calculate number densities for our quiescent sample, as well as for our robust sub-sample (which can be regarded as yielding robust lower limits). We find that the number density of $3 < z < 4$ quiescent galaxies with $F200W < 24.5$ is a factor of 3–5 times higher than previously reported by Schreiber et al. (2018). We demonstrate that this difference arises as a result of better constraints from the new NIRCam data, and show that previously available data from CANDELS would have led us to a similar number density to that calculated by Schreiber et al. (2018). This finding poses an additional challenge for simulations of early galaxy formation, which already struggle to reproduce previously reported number densities.

The 10 robust $z > 3$ massive quiescent galaxies we report, and the 3 at $z > 4$ in particular, are excellent potential targets for follow up NIRSpec spectroscopy, either as part of CEERS, or via dedicated programmes in *JWST* Cycle 2 and beyond. The detection of Balmer absorption features would unambiguously confirm these objects as quiescent at $z > 4$, and full spectral fitting of deep continuum spectroscopic data would provide strong constraints on their SFHs, as well as the ability to probe in detail their physical properties.

[3]https://primer-jwst.github.io

ACKNOWLEDGEMENTS

ACC thanks the Leverhulme Trust for their support via a Leverhulme Early Career Fellowship. RB, DJM, MLH, CD, RJM, JSD, and VW acknowledge the support of the Science and Technology Facilities Council. FC acknowledges support from a UKRI Frontier Research Guarantee Grant (grant reference EP/X021025/1). SMJ and CLP acknowledge the support of the School of Physics & Astronomy, University of Edinburgh via Summer Studentship bursaries.

DATA AVAILABILITY

All *JWST* and *HST* data products are available via the Mikulski Archive for Space Telescopes (https://mast.stsci.edu). Photometric data and fitted model posteriors are available upon request.

REFERENCES

Akins H. B., Narayanan D., Whitaker K. E., Davé R., Lower S., Bezanson R., Feldmann R., Kriek M., 2022, ApJ, 929, 94
Antwi-Danso J. et al., 2022, preprint (arXiv:2207.07170)
Arnouts S., Cristiani S., Moscardini L., Matarrese S., Lucchin F., Fontana A., Giallongo E., 1999, MNRAS, 310, 540
Asplund M., Grevesse N., Sauval A. J., Scott P., 2009, ARA&A, 47, 481
Belli S., Newman A. B., Ellis R. S., 2019, ApJ, 874, 17
Bertin E., 2006, in Gabriel C., Arviset C., Ponz D., Enrique S., eds, ASP Conf. Ser. Vol. 351, Astronomical Data Analysis Software and Systems XV. Astron. Soc. Pac., San Francisco, p. 112
Bertin E., 2010, Astrophysics Source Code Library, record ascl:1010.068
Bertin E., Arnouts S., 1996, A&AS, 117, 393
Beverage A. G., Kriek M., Conroy C., Bezanson R., Franx M., van der Wel A., 2021, ApJ, 917, L1
Brammer G. B., van Dokkum P. G., Coppi P., 2008, ApJ, 686, 1503
Bressan A., Marigo P., Girardi L., Salasnich B., Dal Cero C., Rubele S., Nanni A., 2012, MNRAS, 427, 127
Bruzual G., Charlot S., 2003, MNRAS, 344, 1000
Buchner J. et al., 2014, A&A, 564, A125
Byler N., Dalcanton J. J., Conroy C., Johnson B. D., 2017, ApJ, 840, 44
Calzetti D., Armus L., Bohlin R. C., Kinney A. L., Koornneef J., Storchi-Bergmann T., 2000, ApJ, 533, 682
Carnall A. C. et al., 2019a, MNRAS, 490, 417
Carnall A. C. et al., 2020, MNRAS, 496, 695
Carnall A. C. et al., 2022, ApJ, 929, 131
Carnall A. C. et al., 2023a, preprint (arXiv:2301.11413)
Carnall A. C. et al., 2023b, MNRAS, 518, 45

Carnall A. C., Leja J., Johnson B. D., McLure R. J., Dunlop J. S., Conroy C., 2019b, ApJ, 873, 44
Carnall A. C., McLure R. J., Dunlop J. S., Davé R., 2018, MNRAS, 480, 4379
Castellano M. et al., 2022, ApJ, 938, L15
Cecchi R., Bolzonella M., Cimatti A., Girelli G., 2019, ApJ, 880, L14
Charlot S., Fall S. M., 2000, ApJ, 539, 718
Chevallard J., Charlot S., 2016, MNRAS, 462, 1415
D'Eugenio C. et al., 2021, A&A, 653, A32
Dahlen T. et al., 2013, ApJ, 775, 93
Davé R., Thompson R., Hopkins P. F., 2016, MNRAS, 462, 3265
Dickinson M., FIDEL Team, 2007, in American Astronomical Society Meeting Abstracts. American Astronomical Society, Washington, D.C., United States, p. 52.16
Donnan C. T. et al., 2023, MNRAS, 518, 6011
Esdaile J. et al., 2021, AJ, 162, 225
Falcón-Barroso J., Sánchez-Blázquez P., Vazdekis A., Ricciardelli E., Cardiel N., Cenarro A. J., Gorgas J., Peletier R. F., 2011, A&A, 532, A95
Feroz F., Hobson M. P., Cameron E., Pettitt A. N., 2019, Open J. Astrophys., 2, 10
Finkelstein S. L. et al., 2022, ApJ, 940, L55
Forrest B. et al., 2020, ApJ, 903, 47
Gallazzi A., Bell E. F., Zibetti S., Brinchmann J., Kelson D. D., 2014, ApJ, 788, 72
Gehrels N., 1986, ApJ, 303, 336
Girelli G., Bolzonella M., Cimatti A., 2019, A&A, 632, A80
Glazebrook K. et al., 2017, Nature, 544, 71
Hamadouche M. L. et al., 2022, MNRAS, 512, 1262
Ilbert O. et al., 2006, A&A, 457, 841
Ilbert O. et al., 2013, A&A, 556, A55
Inoue A. K., Shimizu I., Iwata I., Tanaka M., 2014, MNRAS, 442, 1805
Koekemoer A. M. et al., 2011, ApJS, 197, 36
Kroupa P., 2001, MNRAS, 322, 231
Labbe I. et al., 2022, preprint (arXiv:2207.12446)
Leja J., Tacchella S., Conroy C., 2019, ApJ, 880, L9
Marigo P., Bressan A., Nanni A., Girardi L., Pumo M. L., 2013, MNRAS, 434, 488
Marsan Z. C. et al., 2022, ApJ, 924, 25
McLeod D. J., McLure R. J., Dunlop J. S., 2016, MNRAS, 459, 3812
McLeod D. J., McLure R. J., Dunlop J. S., Cullen F., Carnall A. C., Duncan K., 2021, MNRAS, 503, 4413
Merlin E. et al., 2018, MNRAS, 473, 2098
Merlin E. et al., 2019, MNRAS, 490, 3309
Naidu R. P. et al., 2022, ApJ, 940, L14
Pacifici C. et al., 2016, ApJ, 832, 79
Rigby J. et al., 2022, preprint (arXiv:2207.05632)
Salim S., Boquien M., Lee J. C., 2018, ApJ, 859, 11
Sánchez-Blázquez P. et al., 2006, MNRAS, 371, 703
Santini P. et al., 2021, A&A, 652, A30
Schreiber C. et al., 2018, A&A, 618, A85
Skilling J., 2006, Bayesian Anal., 1, 833
Stefanon M. et al., 2017, ApJS, 229, 32
Stevans M. L. et al., 2021, ApJ, 921, 58
Suess K. A. et al., 2022, ApJ, 937, L33
Valentino F. et al., 2020, ApJ, 889, 93
van der Wel A. et al., 2014, ApJ, 788, 28
Wild V. et al., 2014, MNRAS, 440, 1880
Wild V. et al., 2020, MNRAS, 494, 529
Williams R. J., Quadri R. F., Franx M., van Dokkum P., Labbé I., 2009, ApJ, 691, 1879
Wu P.-F. et al., 2018, ApJ, 868, 37

SUPPORTING INFORMATION

Supplementary data are available at *MNRASL* online.

suppl_data

Please note: Oxford University Press is not responsible for the content or functionality of any supporting materials supplied by the authors. Any queries (other than missing material) should be directed to the corresponding author for the article.

APPENDIX A: SEDS AND CUTOUT IMAGES FOR ROBUST QUIESCENT GALAXIES

In Fig. A1, we show SEDs for the seven robust quiescent galaxies we identify at $3 < z < 4$. SEDs for the three robust quiescent galaxies we identify at $z > 4$ are shown in Fig. 1. In Fig. A2, we show 5 arcsec $\times$ 5 arcsec *HST* ACS + *JWST* NIRCam cutout images for each of the 10 galaxies in our robust sample.

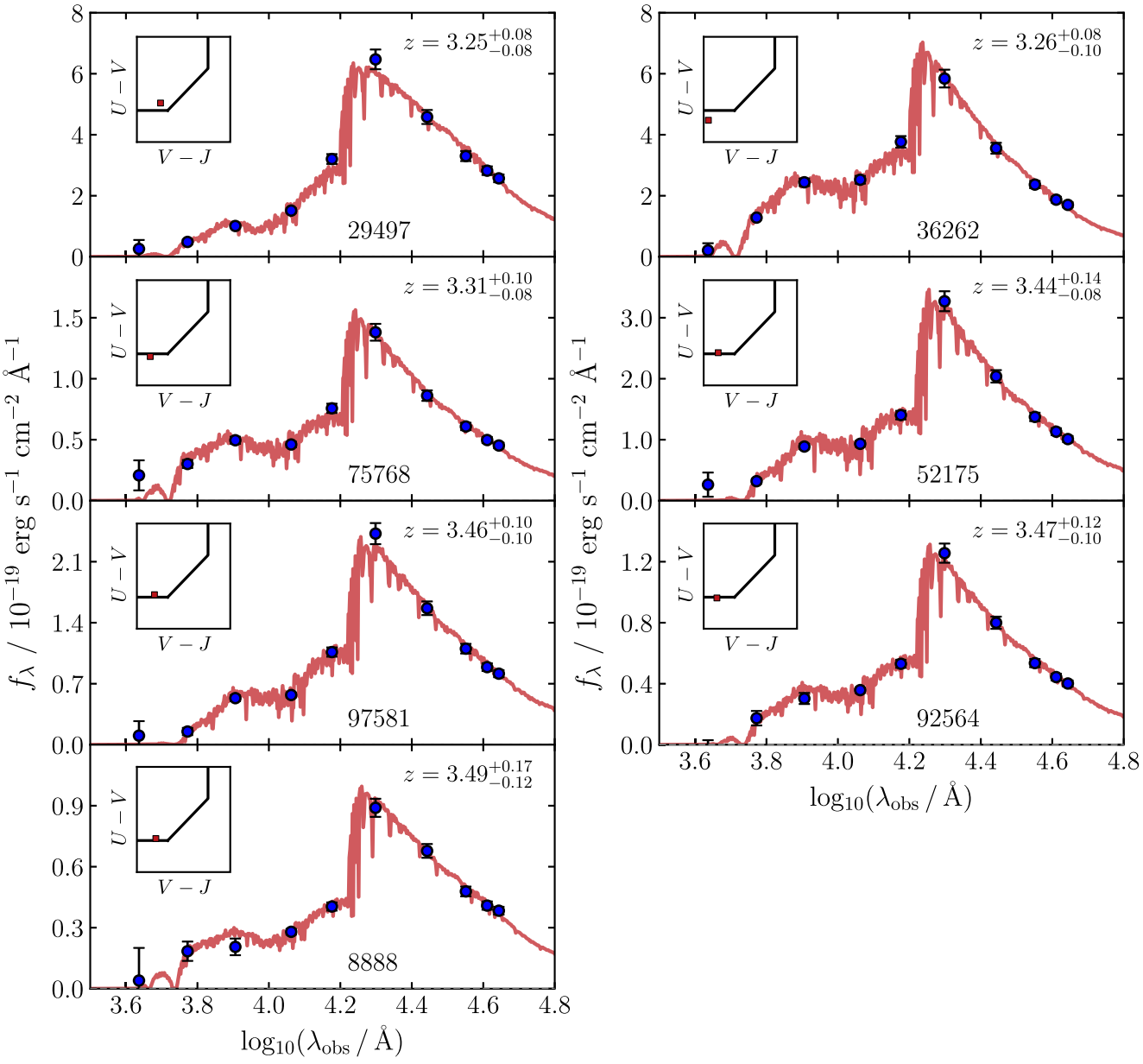

Figure A1. Spectral energy distributions for our seven robust $3 < z < 4$ quiescent galaxies (SEDs for the three robust galaxies at $z > 4$ are shown in Fig. 1). Our 10-band photometric data from *HST* ACS and *JWST* NIRCam are shown in blue. The posterior median BAGPIPES models are overlaid in red. The inset panels show the position of each object on the UVJ diagram.

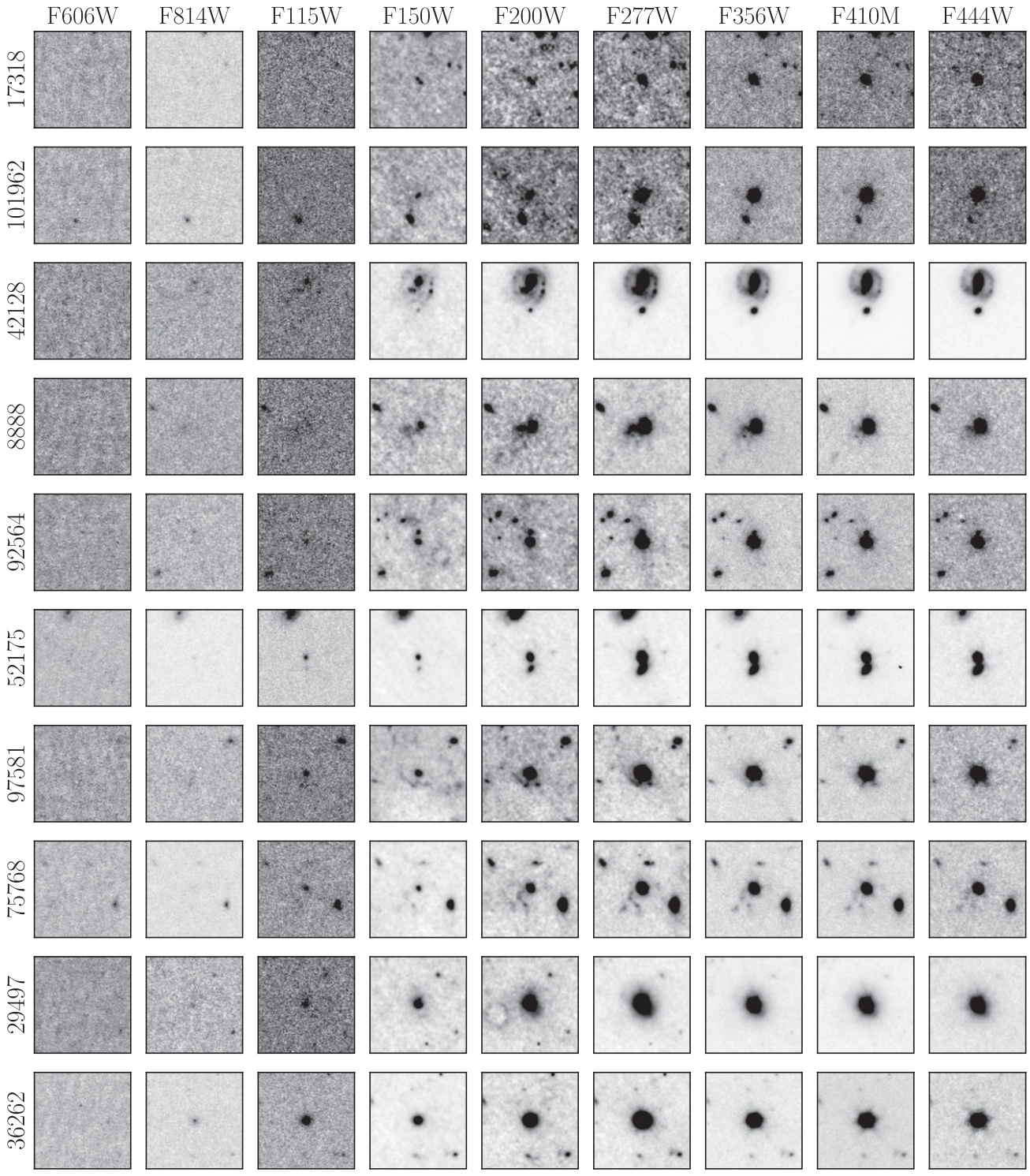

Figure A2. Cutout images for each of the 10 objects in our robust quiescent sample, in descending order of redshift. Each cutout image is 5 arcsec × 5 arcsec.

This paper has been typeset from a TEX/LATEX file prepared by the author.